The role of $\alpha_{IIb}\beta_3$ integrin conformation on the stability and composition of cell adhesions

Application and development of new computational approaches from molecular simulations

Nidhi Soley

Advisor: Tamara C Bidone

Committee: Dr. Chuck Dorval, and Dr. Lucas H Timmins

Abstract

Integrin $\alpha_{IIb}\beta_3$ is an adhesion protein that is expressed at high density on the surface of blood platelets and serves a critical role during arterial thrombosis and hemostasis (1,2). In unstimulated platelets, $\alpha_{IIb}\beta_3$ integrin is held in a bent conformation with almost negligible affinity for extracellular ligands. Upon stimulation and activation of platelets, $\alpha_{IIb}\beta_3$ integrin's affinity for extracellular ligands increases, coincident with a conformational transition into an extended conformation. Activated integrins bind to extracellular ligands, form adhesions and can cause platelet aggregation and blood clotting which leads to thrombotic disorder, stroke, hemorrhage and other cardiovascular diseases (CVD) for which $\alpha_{IIb}\beta_3$ antagonists are in clinical use (2). Mutations that prevent activation of $\alpha_{IIb}\beta_3$ integrin and assembly of adhesions lead to bleeding disorder. Understanding how integrin conformation regulates adhesion assembly and cell function is important to develop new strategies to maintain hemostasis. Previous studies have revealed that conformational extension is essential for integrin to fulfill its cell adhesion function, but how the conformational transitions of $\alpha_{IIb}\beta_3$ integrin exactly affect the dynamics of adhesions remain largely elusive. This is, in part, due to the transient nature of integrin conformations that are intermediate between the bent and extended states and the limited resolution of experimental approaches. In this study, we used a combination of computational methods from atomist simulations to elucidate how the conformations of $\alpha_{IIb}\beta_3$ integrin control the stability and composition of adhesions. Our results indicate that while integrin conformation is responsible for adhesion stability through variations in ligand binding affinity in the first phases of adhesion assembly, it does not determine the composition of adhesions during maturation. These results are conceptually important because they help us identify new functional relationships between integrin conformation and cell function.

Introduction

Almost all cells use adhesion proteins to form a variety of adhesion complexes that range from dynamic to permanent throughout development and homeostasis (1). Adhesion complexes contain transmembrane and cytoplasmic macromolecules to connect the external environment to the cell cytoskeleton. Integrins are a large family of transmembrane heterodimers that mediate the formation of cell-extracellular matrix (ECM) and cell-cell adhesions by directly binding external ligands and intracellular adaptors. Once bound to ligands, integrins recruit a variety of cytoplasmic adaptor proteins, including talin and vinculin, that create the link to the cytoskeleton. Integrins are formed by the noncovalent association of an α and a β subunit, both type I membrane proteins with large extracellular segments, transmembrane helices, and short cytoplasmic tails that bind intracellular adaptors, or integrin-associated proteins (IAPs). Integrins initially bind external ligands to assemble nascent adhesions, which then can stabilize and mature with the recruitment of IAPs. IAPs become extremely concentrated when seen under a microscope during the phase of adhesion maturation (2).

Integrin αIIbβ3 is the major integrin on platelets and regulates platelet aggregation, and thereby, hemostasis and thrombosis (2, 3). The function of αIIbβ3 integrin in platelet aggregation depends upon its capacity to transition from a low to a high affinity state. This transformation allows αIIbβ3 to bind fibrinogen and von Willebrand factor (VWF), ligands that can bridge platelets together, or other ligands, such as vitronectin and fibronectin, which can modulate platelet aggregation (Figure 1) (4). Elucidating the properties of integrin conformation and characterizing their contributions to the assembly and maturation of adhesions is important for understanding the regulation of hemostasis in molecular detail and integrin regulation more generally.

In cells, αIIbβ3 integrins exist in a variety of conformations. In the bent state, the α and β chains are close together, with the upper headpiece bent against the lower headpiece (Figure 2a). In the open, fully extended state, the upper headpiece is separated from the lower

Figure 1. Platelets aggregation: $\alpha_{IIb}\beta_3$ integrins (blue hexagon) is expressed at high density on the surface of blood platelets, when in active or high affinity state it binds to fibrin, fibrinogen (pink rods). These bindings lead to platelet aggregation (4).

headpiece and the α and β chains are apart (Figure 2d). Interconversion between inactive and active states necessarily involve intermediate conformations. Such intermediates have been observed for αIIbβ3 either alone or in association with a ligand (5). They present different degrees of headpiece extension, with the upper headpiece separated from the lower headpiece by different distances, but the lower headpieces and α and β legs together (Figure 2b-c). Intermediate conformations also present different ligand binding affinities and lifetimes of their ligand bound states with respect to both bent and extended conformations. While the inactive/bent and active/extended states of integrin have been described (7,8), less is known about the structure and function of intermediate conformations because of their transient nature.

During maturation of adhesions, integrins recruit a variety of integrin associated proteins (IAPs) acting as linker molecules with the cytoskeleton (10). Talin is one of the most important IAP that directly binds both integrin and the cytoskeleton. The C-terminal rod domain of talin has 13 helical rods, that undergo force-dependent unfolding to expose vinculin binding sites (VBS). Vinculin, a scaffold protein, dynamically links talin to the cytoskeleton. However, it is unclear that how the force-dependent unfolding of talin's 13 helical rods and the binding and unbinding of vinculin exactly affects the maturation of adhesions. This is due to the difficulty in isolating the contribution of each protein experimentally and characterize their emergent effects at the adhesion and cell levels.

In order to understand how αIIbβ3 integrin conformation underlies adhesion assembly and maturation through recruitment of IAPs, here we used a combination of computational methods. We first built all-atom (AA) molecular systems of αIIbβ3 integrins in bent, extended and intermediate conformations and performed equilibrium molecular dynamics simulations. From these simulations, we extracted the collective motions of the residues through principal component analysis (PCA) and evaluated integrin extensional stiffnesses for the different conformations. We incorporated the different integrin conformations into a
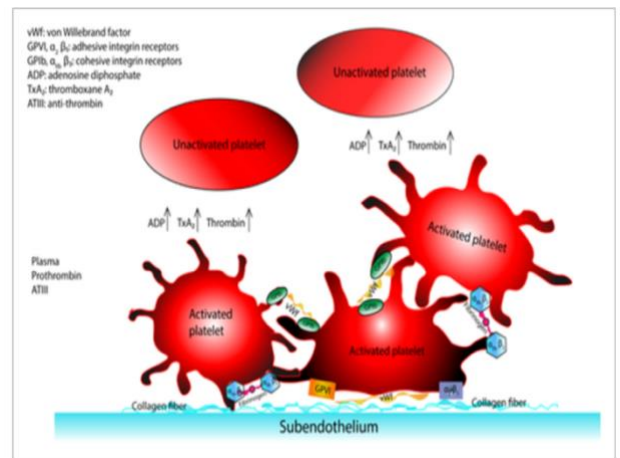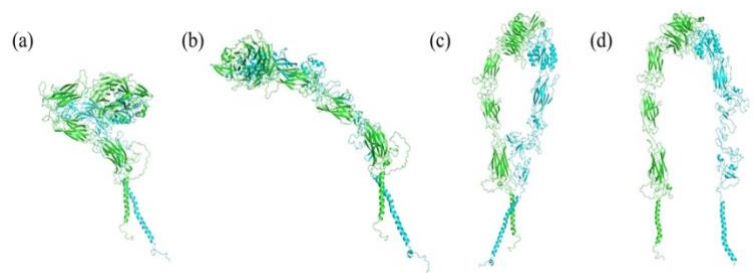
Figure 2. AA $\alpha_{IIb}\beta_3$ integrin and insertion of the missing residues in the bent integrin conformer. Ribbon representation of the AA $\alpha_{IIb}\beta_3$ integrin conformers, with the α chain shown in green and the β chain in cyan: (a) bent; (b) int1; (c) int2; and (d) open conformations.

mesoscale model of adhesion assembly and evaluated their effects on the stability of nascent adhesions. Last, we evaluated the effect of integrin conformation on the composition of adhesions by developing a kinetic model in which integrin and other accessory proteins respond to force by changing their binding and unbinding kinetics. Our results revealed that the conformational deformations of the bent and intermediate states are directed towards elongation of the headpiece away from the legs, and destabilization of the transmembrane helices. The open/extended state presents high flexibility, with correlated motions between headpiece and legs. At the mesoscale, bent integrins cannot form stable adhesions, but intermediate or open conformations stabilize the adhesions. Our results also showed that the different conformations of integrin do not regulate the composition of adhesions during maturation but talin unfolding governs adhesion composition.

Methods

To evaluate the molecular dynamics of $\alpha_{IIb}\beta_3$ integrins in different conformations and assess their effects on the assembly and maturation of adhesions, we combined equilibrium AA simulations, principal components analysis (PCA), Brownian dynamics simulations and kinetic modeling. We started with cryo-EM reconstructions of $\alpha_{IIb}\beta_3$ integrins in the bent, extended and intermediate conformations (Figure 2a-d) and embedded each of these conformers in a lipid bilayer. These structures were purified from human platelets and embedded in lipid nano discs with talin and RGD bound for the cryo-electron microscopy (cryo-EM) study (6). We run 500 ns of equilibrium AA simulations, analyzed the trajectories and calculated the residue fluctuations in order to evaluate differences in dynamics between the different conformations. Then, for each conformation, we characterized the emergent collective motions of the residues and the corresponding extensional stiffnesses using PCA. From analysis of extensional stiffnesses we estimated the activation rates of bent, extended and intermediate $\alpha_{IIb}\beta_3$ conformations and incorporated these parameters into our mesoscale model of adhesion assembly. We used the mesoscale model to study how $\alpha_{IIb}\beta_3$ conformation affects the average percentage of ligand-bound integrins in nascent adhesions and evaluated their stability. Last, we developed a new kinetic model of adhesion maturation and evaluated the composition of adhesions under different forces.

Building lipid bilayer membrane

We reconstructed the missing residues in each of the four $\alpha_{IIb}\beta_3$ cryo-EM reconstructions (6) using Modeller (7) . The completed structures of bent, intermediates (int1 and int2), and open $\alpha_{IIb}\beta_3$ integrin were then embedded within a lipid bilayer using CHARMM-GUI membrane builder (8). The composition of lipid bilayer was 80% DOPC and 20% DOPS with 512 lipids in each leaflet. The integrin/membrane systems were then solvated using CHARMM-modified TIP3P water model (9) and 150 mM NaCl, which served as counter ions to neutralize charges. The resulting solvated systems of membrane-embedded $\alpha_{IIb}\beta_3$ integrins contained approximately: 523,000 total atoms for the bent conformation, 443,000 atoms for int1, 599,000 atoms for int2 and 836,000 atoms for the open conformation.

All Atom molecular dynamics simulations

In order to monitor the dynamic evolution of each $\alpha_{IIb}\beta_3$ integrin conformation, molecular dynamics (MD) simulations were run. First, the systems were energy minimized through steepest descent algorithm, followed by two consecutive equilibration simulations in the constant NVT ensemble (constant number of atoms, *N*, volume, *V*, and temperature, *T*) and four consecutive equilibration simulations in the constant NPT ensemble (constant number of atoms, *N*, pressure, *P*, and temperature, *T*). During the equilibration simulations, positional restrains were applied to both the protein and the lipid heavy atoms, and the dihedral angles. The parameters of these simulations, including the time steps, simulation lengths, and restrains are listed in Table 1. The production runs for 500 ns were then continued in the constant NPT ensemble at 310K and 1 atm. VMD and PyMol were used for the visualization of the simulation trajectories (13,14). Gromacs native analysis tools, combined with our home-made scripts, were employed for the quantitative analysis of the trajectories.

Fluctuation analysis using PCA essential modes

After we obtained 500 ns of equilibrium AA simulation trajectories, PCA was performed on each of the four $\alpha_{IIb}\beta_3$ integrin conformers using Gromacs and batch scripting on the CHPC cluster at the University of Utah. Only the Cα atoms were used in the PCA calculation, and the essential modes were extracted to identify extensional stiffness of each conformer and conformational clusters along the MD trajectories. In order to estimate the extensional stiffness, the distance fluctuations between two groups, the ligand binding site (pulling group) and transmembrane helices (reference group), were calculated as: $D_F = \sum_{k=1}^{M} \lambda^k \left(\sum_{j=xyz} \frac{x_{1j}-x_{2j}}{s} \left(v_{1j}^k - v_{2j}^k \right) \right)^2$, where λ^k and v^k are the eigenvalue and eigenvector of k-th principal mode, s is the distance between the centers of mass (COM) of the pulling and reference groups, and M is the number of essential modes used to evaluate the distance fluctuations. x_j is the x, y or z component of the COM coordinate of each group. v_j is x, y or z component of the eigenvector of each group. The effective force constant describing the extensional stiffness of each conformation was evaluated as $k = \frac{k_B T}{D_F}$, where $k_B T$ = 4.11 pN nm (k_B is the Boltzmann constant, and T is the temperature).
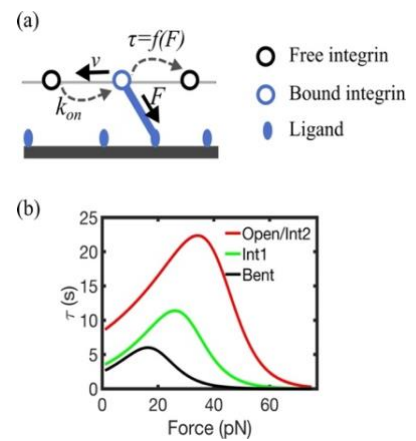
Brownian dynamics simulations of integrin adhesions assembly

To elucidate how integrin conformation affects the assembly of adhesions, we extended our Brownian dynamics model of adhesion assembly (11,13). In the model, two parallel surfaces represent the cell membrane on the top and the substrate on the bottom (schematics in Figure 3a). On the cell membrane, integrins are treated as diffusing particles obeying overdamped Langevin equation, in the limit of high friction, as $F_i - \varepsilon_i \frac{dr_i}{dt} + F_i^T = 0$, where r_i is a position vector of the i-th integrin; ε_i is a friction coefficient equal to 0.0142 pN s/μm, corresponding to the diffusion coefficient of integrin β_3 extracted from single-molecule tracking and super solution imaging, D = 0.29 μm^2/s (11), using Einstein relation $\varepsilon_i = \frac{k_B T}{D}$; dt is the simulation timestep of 10^{-4} s; F_i and F_i^T are deterministic and stochastic forces, respectively.

Figure 3. Brownian dynamics model of adhesions assembly. (a) Schematics of the 2D model of nascent adhesions assembly. (b) Lifetime (τ) versus force relationships for integrin unbinding.

Each diffusive integrin can bind a substrate ligand depending on its activation rate, k_{on}, with probability $P = 1 - e^{-k_{on}dt}$. Once in the ligand-bound state, integrin is subjected to a deterministic force F_i, which is the sum of the force from the retrograde actin flow, and from the interaction with the substrate ligand, F_{sub}, as $F = F_{flow} + F_{sub}$, where $F_{flow} = \varepsilon_i v$, with v = 30 nm/s, and F_{sub} depended on substrate rigidity as $F_{sub} = \frac{YA}{L}\Delta L$, where A is the cross-sectional area of the integrin/ligand bond of 80 nm^2, from an ideal bar of radius ~5 nm corresponding to half the separation between integrin transmembrane legs in the extended active conformation; Y is the substrate's Young's modulus (Y = 12.6 kPa); L is 20 nm is the equilibrium distance between membrane and substrate, comparable to integrin headpiece extension (2), and ΔL is the deviation from the equilibrium distance between the two surfaces (6). The stochastic force on each i-th integrin, F_i^T, represents the thermal force generating Brownian motion, consistent with the fluctuation-dissipation theorem (12): $\langle F_i^T(t)F_j^T(t) \rangle = \frac{2k_B T \varepsilon_i \delta_{ij}}{dt}\delta$ where k_B is the Boltzmann constant, T is the temperature, δij is the Kronecker delta and δ is a unit second-order tensor. Unbinding of integrin from a ligand follows catch bond kinetics, with unbinding rate k_{off} (related to the lifetime as $\tau = \frac{1}{k_{off}}$) including a strengthening pathway with increasing force on the integrin-ligand bond, F, followed by a weakening pathway (13, 14). The catch bond follows a force-dependent Bell model (13) in which

$\tau = f(\mathbf{F})$ (Figure 3b), as follows $k_{off} = A\,e^{-\alpha F} + Be^{\beta F}$. Parameters for catch bond kinetics of each integrin conformer are estimated from (3) and listed in Table 2. Corresponding unbinding probabilities are calculated as $P = 1 - e^{-k_{off}dt}$. The mesoscale model of integrin adhesion assembly reproduces cycles of integrin free diffusion, ligand binding and unbinding. Trajectories of the simulations reproducing integrins' positions in time result from the implementation of explicit Euler integration scheme (14), as $\mathbf{r}_i(t + dt) = \mathbf{r}_i(t) + \frac{d\mathbf{r}_i}{dt}dt = \mathbf{r}_i(t) + \frac{F_i^T + F_i}{\varepsilon_i}dt$.

Kinetic model of adhesion maturation

　　　In order to evaluate the effect of integrin conformation on the recruitment of IAPs, we developed a MATLAB-based kinetic model. The model considers one ligand, one α$_{IIb}$β$_3$ integrin, one talin, and a variable number of vinculins. These proteins bind and unbind one another depending on kinetic rates. In particular, once an integrin binds a ligand, talin can be recruited and bind the cytoskeleton. Depending on the cytoskeletal force, talin can unfold its rods and sequentially expose VBS. Vinculin can bind these sites depending on its association rate, and link to the cytoskeleton. Cytoskeletal force on vinculin determines its unbinding rate.
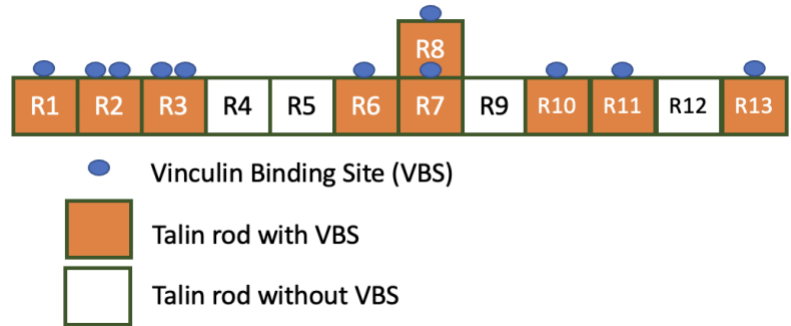
　　　<u>Model initialization.</u> Kinetic parameters for α$_{IIb}$β$_3$ integrin, talin, and vinculin were first initialized based on experimental values (Table 3). As input from the user, the algorithm asks what configuration of α$_{IIb}$β$_3$ integrin need to be considered, between bent, int1, int2/open.

　　　<u>Proteins binding</u> Based on integrin conformation, the algorithm assigns integrin activation rate (Table 3), which is used to determine the probability of binding a ligand. Once integrin is bound to a ligand, the model considers talin association rate and evaluates its binding to actin. Once talin is bound to actin, cytoskeletal force is exerted and results in a sequentially unfold of talin rods exposing VBS. Once VBS are exposed, the binding activity of a maximum of 11 vinculins is evaluated.
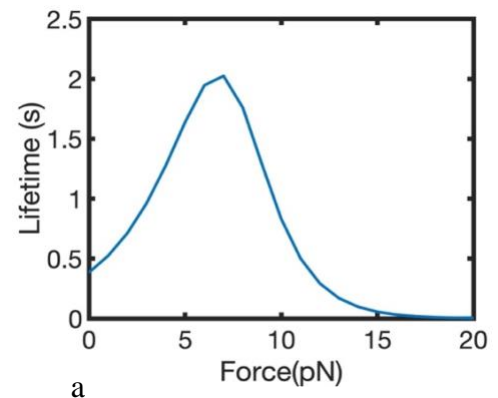

Figure 4. Schematic diagram of 13 talin rods with vinculin binding sites shown in blue dot. The orange box corresponds to the rods that have VBS, white boxes do not have VBS.

　　　<u>Unbinding events</u> After vinculin binds talin, the number of IAPs is calculated and the cytoskeletal force is distributed equally across these elements. Based on the force per elements, the unbinding rate of each IAP and of integrin is calculated. Unbinding of α$_{IIb}$β$_3$ integrin and vinculins follow catch bond kinetics (Figure 3b and Figure 5). For talin, unbinding occurs when the force is above a threshold.

　　　<u>Model iterations and main functions</u> The model is run for 100 s with a time step of 0.01 s. At each iteration, outputs are: the number of IAPs in the adhesion complex, the force per element and the corresponding binding and unbinding rates. We evaluated adhesion composition varying cytoskeletal force between 1-60 pN. The main functions in the code are described below and the code is provided as Appendix.

a

Figure 5. Catch Bond kinetics. Vinculin unbinding rate (inverse of the lifetime) as a function of force follows a Bell shape curve.

- **number_integrin(integrin):** calculates the number of α$_{IIb}$β$_3$ integrins that are bound to a ligand based on integrin activation rate, which depends on integrin conformation (Table 3).
- **number_talin(talin):** calculates the number of talin that are bound to actin based on talin association rate (15).

- **calculate_n_elements(integrin, talin):** calculates the number of integrins and talins resulting from binding and unbinding events.
- **calculate_number_vinculin_bind(n_elements, vinculin,force,talin):** calculates the number of vinculins bound to talin based on: force, unfolding rate of talin rods, available VBS, and vinculin association rate.
- **calculate_force_per_element(n_elements, number_vinculin_bind,force):** calculates the force per element from the total force, as the total cytoskeletal force divided by the number of elements.
- **n_unbound_integrin(integrin,force_per_element): calculates the force-dependent:** determines the number of unbound integrins based on the force per element and the unbinding rate of integrin.
- **n_unbound_talin(talin,force_per_element):** evaluates talin unbinding based on the force on talin.
- **calculate_number_vinculin_unbind(vinculin,force_per_element):** calculated the number of unbound vinculins based on the force per element (Figure 5).

Results

### MD simulations of different integrin conformers in lipid bilayers

In order to evaluate the molecular dynamics of the four conformers of $\alpha IIb\beta 3$ integrin, we ran equilibrium MD simulations for 500 ns (Figure 6). All conformers reached equilibrium within 300 ns (Figure 6a). The Cα root mean square displacements (RMSDs) for bent $\alpha_{IIb}\beta_3$ were between 0.5-1 nm. Cα RMSDs for open $\alpha_{IIb}\beta_3$ leveled off between 2-2.5 nm (Figure 6a). For Int1 and int2, Cα RMSDs reached equilibrium between 1.5-2 nm, intermediate between bent and extended conformers (Figure 6a). These data indicate that bent integrin is conformationally more stable than open integrin, with the intermediate conformations presenting levels of residue fluctuations generally between bent and open states.
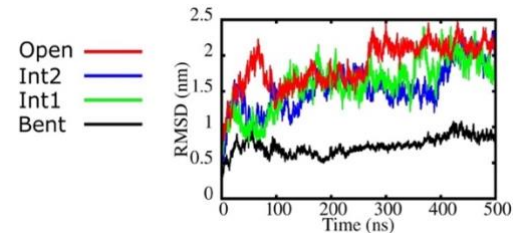
Figure 6. Analysis of AA simulation trajectories of four $\alpha_{IIb}\beta_3$ integrin conformers. (a) The Cα RMSD of the four integrins conformers relative to the corresponding input conformations during 500 ns of AA simulations.

PCA analysis of AA trajectories for different integrin conformers

In order to identify the emergent structural deformations of integrin at the molecular level, PCA analysis was performed. Out of thousands of modes from the large number of residues, only a few modes accounted for about 70 to 90 % of the total fluctuations (Figure 7a). For each mode, the spatial scale of the Cα fluctuations was indicated by the amount of variance, a measure of importance of the fluctuations. The first few modes of all four $\alpha IIb\beta 3$ conformers contained more than 40% of the total variance (Figure 7a). For bent $\alpha IIb\beta 3$ integrin and int1, the first 3 modes contained
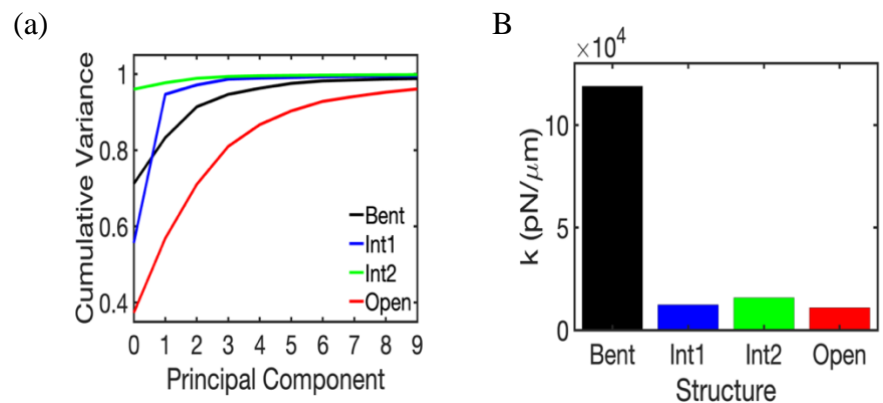

Figure 7. PCA analysis and evaluation of AA fluctuations. (A) Cumulative variance of Cα fluctuations for the four integrin conformations as a function of the principal components from 1 to 10. (B) Extensional stiffness of the four $\alpha_{IIb}\beta_3$ integrin conformers from PCA analysis between 200 ns to 400 ns of equilibrium AA simulations.

more than 95% of the total variance of Cα fluctuations (Figure 7a). For Int2, the first mode contained more than 95% of the total variance (Figure 7a). For open $\alpha IIb\beta 3$ integrin, the first 8 modes contained more than 95% of the total variance (Figure 7a). The effective force constant describing the extensional stiffness of integrin was about 2.5×10^5 pN/µm for bent $\alpha_{IIb}\beta_3$ and ~10x lower for the intermediate and open conformers (Figure 7b).

These data indicate that residues fluctuations fall into a limited number of emergent modes, conferring rigidity to the bent conformation and flexibility to intermediate and open states of integrin.

Identification of conformational clusters from projection of MD trajectories to PCA modes

In order to identify representative structural changes along the PCA modes, we projected the MD simulation trajectories of the four $\alpha_{IIb}\beta_3$ integrin conformers onto the planes identified by the first and second principal modes (Figure 8). For bent $\alpha_{IIb}\beta_3$ integrin, two clusters were identified on the PCA plane (Figure 8a). These clusters differed for a bending motion of integrin headpiece around the membrane-proximal region (Figure 9a). For int1, this analysis identified four clusters (Figure 8b). Comparison between structures of cluster 1 and 2, along the second principal mode, showed opening of the upper headpiece relative to the lower headpiece, with greater distance between the ligand binding site and the legs (Figure 9b). Comparison of clusters 1 and 3 in Int1, along the first principal mode, showed a flattening of the angle between the upper and lower headpieces, without significant variation in the vertical position of the ligand binding (Figure 9b). From the Int2 simulations, two clusters on the PCA plane were identified, along the first mode (Figure 8c). The region containing the ligand binding site twisted around the integrin's longitudinal axis, combined with further lengthening of the headpiece and changes in the orientation of trans-membrane β helix (Figure 9c). For open $\alpha_{IIb}\beta_3$, we three clusters were found on the PCA plane. Integrin headpiece was highly flexible, presenting collective pivoting of the upper headpiece relative to the lower headpiece for αIIb and of the whole headpiece relative to the legs for β3 (Figure 9d). Both transmembrane helices also changed orientation relative to the membrane plane, in the direction to maintain their alignment relative to the main axis of the headpiece (Figure 9d). Notably, our results showed that while the bent and the first intermediate conformations of $\alpha_{IIb}\beta_3$ integrin only moved the headpiece, the second intermediate and open conformers also moved the legs. Therefore, the order of conformational changes from bent to extended states starts from the headpiece and is then transmitted to the legs. In the initial intermediate conformation, the flattening of the headpiece and its extension in the vertical direction are independent motions, while in the second intermediate the twisting of the extracellular ligand
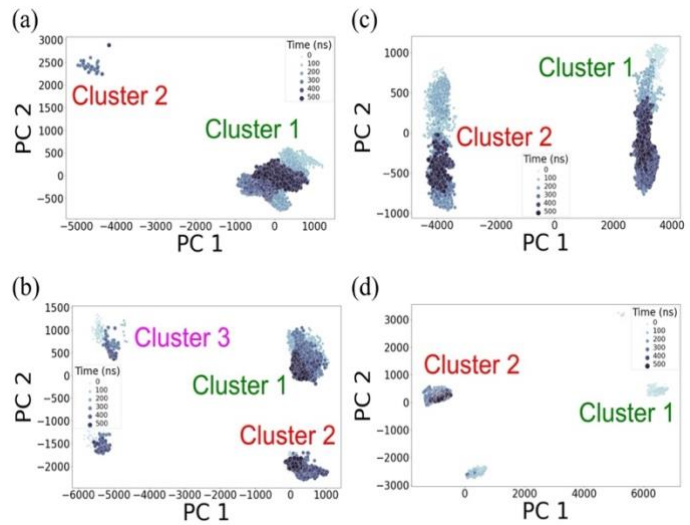
Figure 8. Projection of simulation trajectories to the first two PCA modes and alignments of representative structures from identified clusters (a-d). The scatter plots of simulation frame projections are colored by their simulation times, and the clusters are indicated with green, red and magenta for cluster 1, 2 and 3, respectively.
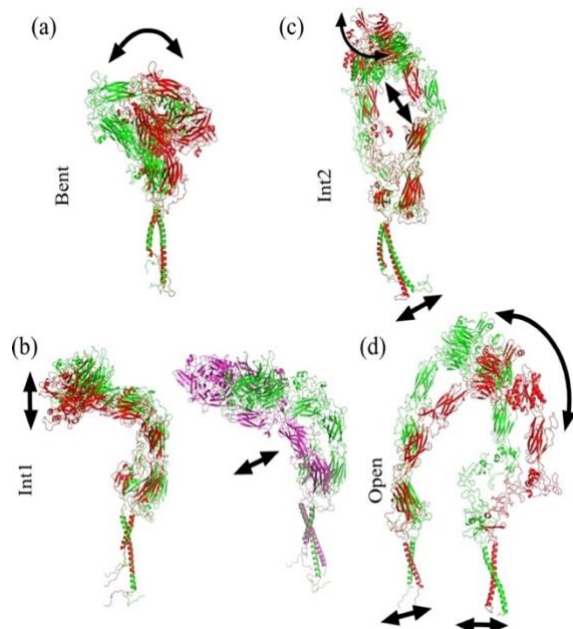
Figure 9. Representative structures from clusters identified on the plane of the first two principal modes. (a) Superposition of the representative AA structures from clusters 1 and 2 in the bent states. (b) int1. (c) int2. (d) open.

binding site, the extension of the headpiece and leg separation are all correlated motions. These correlations, in which elongation of the headpiece is combined with movement of its ligand binding interface and reorientation of the β helix, are likely to underlie the coordinated binding of an external ligand and accessory cytoplasmic proteins.

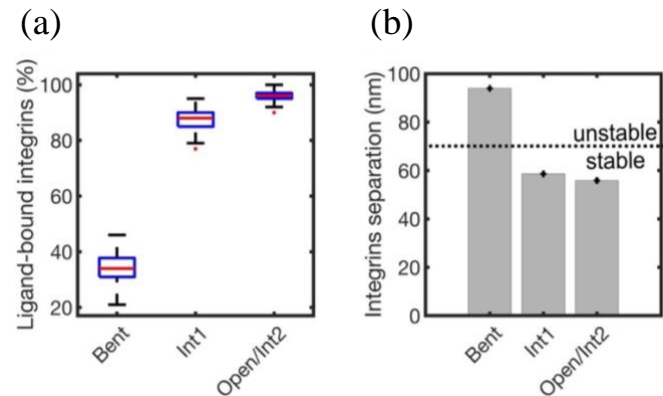**Brownian dynamics simulations of integrin adhesion assembly**

We next assessed the effect of $\alpha_{IIb}\beta_3$ integrin conformation on the assembly of adhesions by incorporating different integrin conformers into a mesoscale model (schematics in Figure 3a). In this model, integrins undergo cycles of diffusion in the membrane, and binding and unbinding of matrix-anchored ligands. Binding to ligands is described by an activation rate k_{on}, extracted from PCA, while unbinding is described by force-dependent lifetimes of the ligand-bound state (Figure 3b). Force on ligand-bound integrins is generated by actin retrograde flow and substrate stiffness (Figure 3a). Simulation runs incorporated values of k_{on} and τ_{MAX} representing each $\alpha_{IIb}\beta_3$ integrin conformer. For the bent conformer $k_{on} = 0.07$ s^{-1} and $\tau_{MAX} = 6$ s; for int1 $k_{on} = 0.7$ s^{-1} and $\tau_{MAX} = 11$ s; for Int2 and the open conformers $k_{on} = 1$ s^{-1} for and $\tau_{MAX} = 22$ s. Results showed that the distribution of ligand-bound integrins shifted toward higher values as integrin conformation

Figure 10. Integrin conformation determines the density of ligand-bound integrins in nascent adhesions. (a) Boxplots of ligand- bound integrins for the different integrin conformations with force corresponding to τ_{max} around 40 pN. (b) Average smallest distance between ligand-bound integrins. Errorbars represent standard deviation from the mean. For all the analysis data were extracted between 200 s and 300 s of simulations, using 300 ligands/μm2 and Y=12.6 kPa.

shifted from bent to extended (Figure 10 a). Additionally, the distribution of bound integrins narrowed from bent to extended states (Figure 10 a), with less variability in the amount of ligand binding at high affinities (high k_{on}) and high ligand-bound lifetimes (low k_{off}, or high τ_{MAX}). Consistent with a greater number of ligand-bound integrins, the average minimum distance between ligand-bound integrins was larger than 90 nm for bent integrin and less than 60 nm for intermediate and open $\alpha_{IIb}\beta_3$ conformers (Figure 10b), indicating greater density of ligand bound integrins in the plasma membrane. Based on the experimentally identified threshold of 70 nm for adhesion stabilization (22), our results indicated that the probability of adhesion stabilization is high for intermediate and open integrins, and low for bent integrins. Collectively, the results from mesoscale modeling showed that bent $\alpha_{IIb}\beta_3$ fails to stabilize nascent adhesions, whereas conversion to the intermediate states promotes adhesion stability nearly (Int1) or as well (Int2) as the fully open conformation. This implies that the force from binding ligands on the substrate can convert integrin conformation from partially open to fully open.

Effects of integrin conformation on adhesions composition

In order to evaluate the composition of adhesions as a function of cytoskeletal force, we developed a kinetic model. From this model, no difference in adhesion composition was detected using different conformations of αIIbβ3 integrin (Figure 11a). Increasing the force from 1 pN to 60 pN resulted in an increase in the number of elements in the adhesion, from 3-4 total elements, including integrin, talin and vinculin, at low values of pN, up to 13 elements at about 60 pN. All four conformations of integrin responded to force by recruiting approximately the same number of elements for similar force ranges: below 18 pN, about four elements were present in the adhesion, including integrin, talin and 2 vinculins; for forces between 19-33 pN, a total of seven elements were present, including vinculin, talin and 5 vinculins; in the range of force between 33-

42 pN, about 11 elements were present, corresponding to one integrin, one talin and 9 vinculins; above 42 pN, 13 elements were present in the adhesion, including one integrin, one talin and 11 vinculins. These stepwise increases in the average number of adhesion elements, from 4 to 7 to 11 and 13, indicated that adhesion maturation follows the discrete unfolding events of talin rods. Our results also showed that, more than 2 elements are present in the adhesion at all force values; by contrast, for forces below 20 pN, the frequency of having more than 10 elements was significantly lower. As force is increased from 21 pN to 40 pN, the frequency of obtaining a number of elements larger than 10 increased from 0.01 to 0.55; in the force range 41-60 pN, more than 10 elements were present in 100% cases (Figure 11 B). This signifies that while vinculin is readily available to be recruited to integrin adhesions, its density increases significantly only at large forces.

Figure 11. Adhesion composition as function of force. A) Maximum number of elements for each value of force, error bars show standard deviation. B) Frequency of occurrence of the specific number of elements in three force ranges.

Discussion

Classical integrins, including β1, β2, β3, and β7 integrins, that associate with talins and vinculins, transition from bent, low affinity to extended, high affinity states through intermediate conformations. These conformation influence adhesion assembly and maturation and cell adhesive functions (2,4,11, 14). However, the molecular properties of these states and their roles in the assembly and maturation of adhesions remain largely elusive. In this study, we combined molecular simulations, principal components analysis, mesoscale and kinetic modeling approaches in order to evaluate the structural motions of integrin αIIbβ3 in different conformations and their role in cell adhesion assembly and maturation.

Our results indicated that, in the absence of extracellular or intracellular ligand binding, conformational fluctuations of αIIbβ3 integrin are enhanced in the intermediate and open conformations as compared to the bent conformation. Mesoscale modeling further identified a mechanism linking the conformational transitions of integrin to stabilization of nascent adhesions. This result, when linked to the aggregation of platelets as a response to vascular damage, implies that the inactive/ bent state of integrin is capable of aggregating platelets and forming clots when ligands like fibrin, fibrinogen is attached to it for a long period of time. However, these adhesions are not stable.

PCA-based analysis of αIIbβ3 integrin in the four conformations indicated that most molecular fluctuations are contained along a very limited number of principal modes (Figure 7a). A few principal modes contained between 70 and 80% of the total residue fluctuations. These modes occurred as collective displacements of the residues in the directions of knee flattening, headpiece extension and leg separation. Interestingly, these modes of deformations varied significantly between the different αIIbβ3 integrin conformations, with independent uncoupled motions in the first intermediate and coupled deformations between headpiece and legs for the more extended intermediate and the open state. Our lab has previously shown that force promotes integrin conformational activation, depending upon the exact molecular structure and corresponding activating mutant (10). It is plausible that the different modes of deformation that are associated with the different molecular structures of integrin underlie different structural responses to force. It would be interesting to evaluate, in the future, how the mutants perturb these modes of motion.
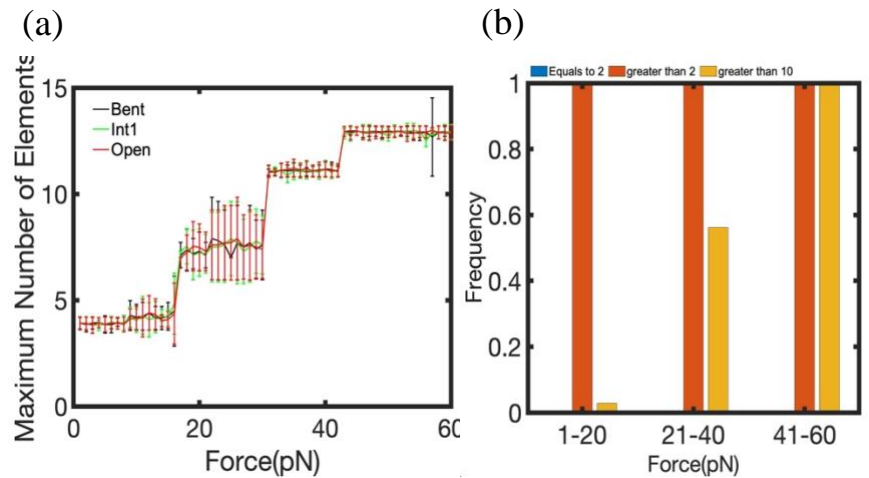
Using the principal modes and the results from PCA analysis we evaluated the flexibility of the αIIbβ3 integrin conformers. The bent/ inactive state presented the highest extensional stiffness while the open/active conformation presented the lowest stiffness, which signifies that in absence of ligand binding the bent/inactive state is the most rigid and the open state the most flexible across conformations.

Through the PCA cluster analysis we deduced the structural changes occurring in the four αIIbβ3 integrin conformers along the two principal components. Identification of conformational clusters along the principal components of integrin motion suggests that headpiece extension and leg separation occur sequentially during conformational activation, as previously proposed (12). In particular, the uncoupled motions of the headpiece are transmitted to the β leg first and then to the α leg, resulting in allosteric coupling between headpiece and legs. In the bent and first intermediate states, only motions of the headpiece were observed. Additionally, in the first intermediate, headpiece extension in the vertical direction proceeds independently from flattening of the angles between upper and lower headpiece. In the later phases of activation, corresponding to the second and open states, the rearrangements of the headpiece, including exposure of its ligand binding site, separation between the upper α and β chains, and legs opening are coupled.

Mesoscale modeling identified a mechanism linking integrin conformational transitions to stabilization of nascent adhesions. According to this model, bent integrins can bind ligands with low affinity, but short bond lifetimes prevent adhesion stabilization. As the integrin headpiece extends and ligand binding affinity increases, the probability of ligand binding increases and once bound, a concomitant increase in bond lifetime confer stability to the nascent adhesions. Therefore, increases in integrin affinity across intermediates stabilize nascent adhesions via increase in the duration of the integrin-ligand bond. While our analysis focused on αIIbβ3, these principles are likely applicable to other integrins that show similar conformational activation.

Kinetic modeling of adhesion maturation through recruitment of IAPs proteins showed that integrin and talin are present in adhesions both with and without cytoskeletal force. By contrast, vinculin is recruited in a stepwise fashion, which depends on the discrete unfolding events of the talin rods. As a force of few pN is applied, at least 2 vinculins bind talin. This occurs because of the lower unfolding rate of rod 3 (R3) of the talin rod, that unfolds at a force range of 0-8 pN (10) and makes 2 VBS accessible for vinculin. For higher force values, more elements are recruited in the adhesion, leading to strengthening and maturation. This result signifies that as the force increases, more and more vinculins bind and the force on the entire system is distributed over more IAPs, resulting in reduced force per element. This allows αIIbβ3 integrin and talin to remain bound even at force values of the order of several tens of pN (Figure 11b).

This study leads to **three main conclusions of high novelty**. First, the combination of simulation from the molecular to the mesoscale levels allowed us to isolate the emergent motions of integrin in different conformations. The development of a new kinetic model allowed us to evaluate how these conformations further affect adhesion reinforcement through recruitment of IAPs. Our results collectively demonstrate that, in the absence of ligand binding, the motions of the headpiece of integrin precede the motions of the legs and that fluctuations of the β transmembrane helix precedes those of the α helix. The initial headpiece motions can be related to early increases in ligand binding affinity upon destabilization of the bent conformation which are not reflected by significant headpiece extension (12). The motions that are transmitted from the headpiece to the β transmembrane helix are likely important for binding of accessory cytoplasmic proteins, connection with the cytoskeleton and intracellular signaling. Second, our results identify a new mechanism by which small changes in affinity are transduced into adhesion stabilization through control of the molecular integrin-ligand catch bond. The importance of the ligand-bond lifetime in adhesion stabilization has previously been reported from studies of cell spreading on substrates with different rigidities (35, 50), but has not been investigated in relation with integrin conformation. Third, integrin conformation does not affect recruitment of IAPs, but the

discrete nature of talin rod unfolding under force determines adhesion maturation and strengthening. These results are consistent with the view of talin as the "master" of adhesions, because of its role in coordinating kinetics activities of integrin, vinculin and cytoskeleton (17).

Our new results raise a number of questions that remain to be addressed in future work. While we have investigated how integrin conformation affects adhesion stabilization and IAPs recruitment, how exactly the binding of IAPs affect integrin conformation remains unexplored. Similarly, how the binding of IAPs regulates integrin clustering versus affinity remains to be explored in future work (22). Additionally, since substrate rigidity plays an important role in integrin conformational activation and ligand-bound lifetime (18), it will be interesting to test the effect of substrate stiffness on adhesion assembly and maturation through conformational changes of integrin and recruitment of IAPs.

References

1.   Xiong, J.P., T. Stehle, B. Diefenbach, R. Zhang, R. Dunker, D.L. Scott, A. Joachimiak, S.L. Goodman, and M.A. Arnaout. 2001. Crystal structure of the extracellular segment of integrin alpha Vbeta3. *Science (New York, N.Y.)*. 294:339–45.

2.   Humphries JD, Byron A, Humphries MJ. Integrin ligands at a glance. J Cell Sci. 2006 Oct 1;119(Pt 19):3901-3. doi: 10.1242/jcs.03098. PMID: 16988024; PMCID: PMC3380273.

3.   Chen, Y., L.A. Ju, F. Zhou, J. Liao, L. Xue, Q.P. Su, D. Jin, Y. Yuan, H. Lu, S.P. Jackson, and C. Zhu. 2019. An integrin α(IIb)β(3) intermediate affinity state mediates biomechanical platelet aggregation. *Nature materials*. 18:760–769.

4.   Ma YQ, Qin J, Plow EF. Platelet integrin alpha(IIb)beta(3): activation mechanisms. J Thromb Haemost. 2007 Jul;5(7):1345-52. doi: 10.1111/j.1538-7836.2007.02537.x. PMID: 17635696

5.   Driscoll, T.P., T.C. Bidone, S.J. Ahn, A. Yu, A. Groisman, G.A. Voth, and M.A. Schwartz. 2021. Integrin-based mechanosensing through conformational deformation. *Biophysical journal*. 120:4349–4359.

6.   Xu, X.-P., E. Kim, M. Swift, J.W. Smith, N. Volkmann, and D. Hanein. 2016. Three-Dimensional Structures of Full-Length, Membrane-Embedded Human α(IIb)β(3) Integrin Complexes. *Biophysical journal*. 110:798–809.

7.   Fiser, A., R.K. Do, and A. Sali. 2000. Modeling of loops in protein structures. *Protein science : a publication of the Protein Society*. 9:1753–1773.

8.   Jo, S., J.B. Lim, J.B. Klauda, and W. Im. 2009. CHARMM-GUI Membrane Builder for Mixed Bilayers and Its Application to Yeast Membranes. *Biophysical Journal*. 97:50–58.

9.   Jorgensen, W.L., J. Chandrasekhar, J.D. Madura, R.W. Impey, and M.L. Klein. 1983. Comparison of simple potential functions for simulating liquid water. *The Journal of Chemical Physics*.

10. Yao, M., Goult, B., Klapholz, B. et al. The mechanical response of talin. Nat Commun 7, 11966 (2016). https://doi.org/10.1038/ncomms11966

11. Rossier, O., V. Octeau, J.-B. Sibarita, C. Leduc, B. Tessier, D. Nair, V. Gatterdam, O. Destaing, C. Albigès-Rizo, R. Tampé, L. Cognet, D. Choquet, B. Lounis, and G. Giannone. 2012. Integrins β1 and β3 exhibit distinct dynamic nanoscale organizations inside focal adhesions. *Nature Cell Biology*. 14:1057–1067.

12. Kubo, R. 1966. The fluctuation-dissipation theorem. *Reports on Progress in Physics*. 29:255–284.

13. Bell, G.I. 1978. Models for the specific adhesion of cells to cells. *Science*.

14. 2016. Differential and Difference Equations. *Numerical Methods for Ordinary Differential Equations*. 1–53.

15. Goldmann WH, Isenberg G. Kinetic determination of talin-actin binding. Biochem Biophys Res Commun. 1991 Jul 31;178(2):718-23. doi: 10.1016/0006-291x(91)90167-6. PMID: 1907136. Selhuber-Unkel, C., M. López-García, H. Kessler, and J.P. Spatz. 2008. Cooperativity in adhesion cluster formation during initial cell adhesion. *Biophysical journal*. 95:5424–5431.

16. Coutinho, A., C. García, J. González-Rodríguez, and M.P. Lillo. 2007. Conformational changes in human integrin alphaIIbbeta3 after platelet activation, monitored by FRET. *Biophysical chemistry*. 130:76–87.

17. Klapholz B, Brown NH. Talin - the master of integrin adhesions. J Cell Sci. 2017 Aug 1;130(15):2435-2446. doi: 10.1242/jcs.190991. Epub 2017 Jul 12. PMID: 28701514.

18. Oakes, P.W., T.C. Bidone, Y. Beckham, A.V. Skeeters, G.R. Ramirez-San Juan, S.P. Winter, G.A. Voth, and M.L. Gardel. 2018. Lamellipodium is a myosin-independent mechanosensor. *Proceedings of the National Academy of Sciences of the United States of America*. 115.

19. Xu, X.P., E. Kim, M. Swift, J.W. Smith, N. Volkmann, and D. Hanein. 2016. Three-Dimensional Structures of Full-Length, Membrane-Embedded Human ??iIb??3 Integrin Complexes. *Biophysical Journal*. 110:798–809.

20. Wiograd-Katz SE, Fässler R, Geiger B, Legate KR. The integrin adhesome: from genes and proteins to human disease. Nat Rev Mol Cell Biol. 2014 Apr;15(4):273-88. doi: 10.1038/nrm3769. PMID: 24651544.

21. Haining AW, Lieberthal TJ, Del Río Hernández A. Talin: a mechanosensitive molecule in health and disease. FASEB J. 2016 Jun;30(6):2073-85. doi: 10.1096/fj.201500080R. Epub 2016 Feb 22. PMID: 27252130.

22.   Goldmann WH, Isenberg G. Kinetic determination of talin-actin binding. Biochem Biophys Res Commun. 1991 Jul 31;178(2):718-23. doi: 10.1016/0006-291x(91)90167-6. PMID: 1907136. Selhuber-Unkel, C., M. López-García, H. Kessler, and J.P. Spatz. 2008. Cooperativity in adhesion cluster formation during initial cell adhesion. *Biophysical journal*. 95:5424–5431.

23.   Yinan Wang, Mingxi Yao, Karen B. Baker, Rosemarie E. Gough, Shimin Le, Benjamin T. Goult, and Jie Yan *Journal of the American Chemical Society* 2021 *143* (36), 14726-14737
      DOI: 10.1021/jacs.1c06223

24.   Huang DL, Bax NA, Buckley CD, Weis WI, Dunn AR. Vinculin forms a directionally asymmetric catch bond with F-actin. Science. 2017 Aug 18;357(6352):703-706. doi: 10.1126/science.aan2556. PMID: 28818948; PMCID: PMC5821505.

25.   Hirata H, Tatsumi H, Hayakawa K, Sokabe M. Non-channel mechanosensors working at focal adhesion-stress fiber complex. Pflugers Arch. 2015 Jan;467(1):141-55. doi: 10.1007/s00424-014-1558-3. Epub 2014 Jun 26. PMID: 24965068

Appendix

List of Tables:

Table 1. Details of equilibrium simulations. The last four columns are the force constants (FC) for positional restraint of protein backbone atoms, protein side chain atoms and lipid heavy atoms, as well as dihedral restrains of lipid molecules used in different stages of equilibration simulations. The unit of force constants are $kJ/(mol \cdot nm^2)$.

Step	Length	FC_BB	FC_SC	FC_LIPID	FC_DIHRES
1	250ps	4000	2000	1000	1000
2	250ps	2000	1000	400	400
3	250ps	1000	500	400	200
4	500ps	5000	200	200	200
5	500ps	200	50	40	100
6	500ps	50	0	0	0

Table 2. Parameters for catch bond kinetics of different αIIbβ3 integrin conformers, estimated from (1).

Integrin conformer	A	B	α	β
Bent	0.4	0.5E-2	0.08	0.15
Int1	0.3	0.5E-3	0.06	0.15
Open/Int2	0.12	0.5E-4	0.035	0.15

Table 3. Parameters of talin and vinculin.

Integrin	Bent	Int1	Open/Int2
Activation Rate (s^{-1})	0.07	0.7	1
Talin			
Talin_actin association rate(s^{-1}) (15)	Rate ($M^{-1}s^{-1}$) 7 x 10^6 in concentration of 1.4 µM. Rate(s^{-1}) 9.8		
Maximum force on talin (pN) (10)	10		
Vinculin			
Vinculin_talin association rate(s^{-1}) (23)	Rate ($M^{-1} s^{-1}$) 1.0±0.4 × 10^6 in the concentration of 10nM. Rate(s^{-1}) 0.01.		
Parameters for catch bond kinetics (24)	**A**=2.6, **B**=0.4E-2, α=0.312, β=0.560		

Table 4. Unfolding rate of talin rod domains in s^{-1} (10).

Talin rod domain	1	2	3	4	5	6	7-8	9	10	11	12	13
Unfolding rate (s^{-1})	4.2E-6	1.7E-8	0.018	4.2E-6	2.5E-5	2.5E-5	4.2E-6	4.2E-6	2.5E-5	2.5E-5	1.7E-8	2.5E-5

Table 5. Number of VBS accessible for four group of forces in pN (10).

Force (pN)	0 to <8	8 to <15	15 to <21	>21
Number of VBS (count)	2	3	4	2